Focus-engineered coherent anti-Stokes Raman scattering microscopy: a numerical investigation

Vishnu Vardhan Krishnamachari and Eric Olaf Potma

Department of Chemistry and Beckman Laser Institute, University of California at Irvine, Irvine, California 92697, USA

Received September 18, 2006; revised October 31, 2006; accepted October 31, 2006; posted November 2, 2006 (Doc. ID 75135); published March 14, 2007

The coherent anti-Stokes Raman scattering (CARS) signal is calculated as a function of focal-field distributions with engineered phase jumps. We show that the focal fields in CARS microscopy can be shaped such that the signal from the bulk is suppressed in the forward detection mode. We present the field distributions that display enhanced sensitivity to vibrationally resonant object interfaces in the lateral dimension. The use of focus-engineered CARS provides a simple means to detect chemical edges against the strong background signals from the bulk. © 2007 Optical Society of America

OCIS codes: 190.4380, 270.1670, 180.5810, 140.3300.

1. INTRODUCTION

Coherent anti-Stokes Raman scattering (CARS) microscopy is an increasingly popular imaging tool for chemical mapping of biological cells and tissues,[1–4] as it offers excellent chemical selectivity,[5] optical sectioning capability,[6] and high sensitivity.[7] The detected signal in a CARS microscope is a result of coherent superposition of the signal waves generated in the focus.[8,9] Thus, unlike the output from incoherent processes such as fluorescence, the CARS signal is shaped by the constructive and destructive interference of the CARS waves emanating from the focal volume. The interference nature of CARS is particularly evident in the epidirection (or backward-propagating direction), where the waves typically destructively interfere unless subwavelength objects or interfaces are present.[10,11] It is this interference effect that gives rise to the size-selective imaging properties of epi-CARS. Detection in the epimode has proven useful for high-contrast imaging of small cell structures, such as lipid droplets, interfaces, etc. On the other hand, the forward CARS signal, which can be 2 orders of magnitude greater than the backward signal, is not size selective and hence the signals from both the bulk as well as those from the smaller objects are detected in the forward mode.

It is important to note that the interference effect in epi-CARS is prominent only along the longitudinal direction (i.e., along the optical axis) but not in the lateral direction. Hence epi-CARS is not sensitive to the interfaces or $\chi^{(3)}$ discontinuities in the lateral dimensions. In cellular imaging, it is often necessary to differentiate between various cellular features such as vacuoles, lipids, cell membrane, etc., at the plane of focus. In this paper, we explore the possibility of suppressing the bulk contribution from the sample and detecting, along the forward direction, the chemical edges and/or interfaces present in the lateral plane. We show that such CARS imaging properties can be achieved by shaping the spatial profile of the excitation field at the focus.

The concept of focus engineering or point-spread function engineering[12] has been used in fluorescence microscopy with great success. With the techniques of stimulated-emission depletion[13,14] and 4Pi microscopy,[15,16] which rely on engineering the amplitude distribution of the excitation field near the focus, spatial resolution of the order of a few tens of nanometers has been achieved.[17] It has also been lately employed in wide-field conventional microscopy for detecting phase and amplitude jumps in the field of view.[18] However, to date, no effort has been made to implement this concept in CARS microscopy. Since CARS is a coherent process, it is expected that the resulting signal is particularly sensitive to the phase profile of the excitation fields. It is known, for instance, that asymmetric beam mode combinations in optical waveguides have a strong influence on the generated CARS signal.[19] By engineering the focal field, we show that the far-field CARS signal becomes highly sensitive to vibrationally resonant interfaces or subwavelength-sized objects, and that the CARS signal is devoid of the background from the bulk. Although there are other nonlinear microscopy techniques, such as second-harmonic generation microscopy[20–23] and third-harmonic generation microscopy,[24–27] which efficiently reduce the bulk background and highlight only the sub-wavelength-sized objects or interfaces, the chemical specificity offered by focus-engineered CARS makes it a more versatile tool for analyzing the spectroscopic properties of biological samples.

In this paper, we report a systematic investigation of focus-engineered CARS signals for a variety of sample geometries. To simulate focal fields with well-defined phase steps, we employ tightly focused Hermite–Gaussian beams. We show that the phase profiles of such higher-order beam modes enable background suppression and highlight the chemical edges in lateral dimensions. In addition, we address the spectral dependence of the focus-engineered CARS output and demonstrate that under cer-

tain conditions, the CARS spectrum of these edges resembles the Raman spectrum. Finally, we discuss two modes of detection of the CARS signal—the incoherent and the coherent detection schemes—the latter of which leads to further enhancement in the contrast of the interfaces.

2. QUALITATIVE DESCRIPTION OF THE IDEA

Figure 1 shows the basic configuration of CARS generation at the focal volume in a homogeneous medium. The Stokes and the pump beams of angular frequencies ω_S and ω_p are focused using a large numerical aperture lens. The CARS waves are generated at different points in the excitation volume with their amplitudes proportional to the local excitation fields and their phases ϕ_c being related to the local phases of the pump, ϕ_p, and the Stokes fields, ϕ_S as $\phi_c = 2\phi_p - \phi_S$. Let P be a generic point in the focal volume and Q be a point in the far field where the CARS intensity is detected. Then, the CARS field at Q is the sum of the field contributions from all the points, such as P, in the focal volume. In a conventional CARS microscope, where tightly focused Gaussian beams are used for excitation, the CARS intensity is maximum closer to the optical axis (near O') and reduces gradually away from it. This is explained by considering the interference of the CARS waves generated at two points, A and B, which are equally separated from the optical axis (along the y direction). The waves arriving at O' from the points A and B are in phase with respect to each other due to equal optical paths ($\overline{AO'}$ and $\overline{BO'}$) traversed by them and hence interfere constructively. On the other hand, the waves arriving at an off-axis point Q will not be completely in phase due to the asymmetry in the path lengths $\overline{AQ}$ and $\overline{BQ}$. Thus, in general, with Gaussian excitation, the far-field CARS intensity is greatest near the optical axis.

Let us consider the situation in which the CARS signal generated in the upper half (the region corresponding to $y>0$) of the focal volume is π out of phase with respect to that generated in the lower half ($y<0$). Then, based on the above discussion, due to the destructive interference between the waves propagating from points such as A and B in Fig. 1, the intensity at O' should be minimum. On the other hand, for off-axis far-field points, the CARS intensity increases and may reach a maximum when the optical path difference between the individual interfering waves tends to π rad. Thus, if the CARS intensity from the region close to the optical axis is detected (as in a conventional CARS microscope), the net CARS output would be negligibly small even if the bulk sample is highly resonant. Such a detection scheme would thus allow for the suppression of the bulk contributions in the forward CARS. Note that this suppression is obtained by manipulating the phase distribution in the focal volume and is a direct manifestation of the coherent nature of the CARS process; this phenomenon cannot be observed with incoherent processes such as fluorescence.

Consider next an interface formed between two spectroscopically different materials, or equivalently, materials with different third-order nonlinear susceptibilities, with $\chi^{(3)}=\chi_1$ for $y>0$ and $\chi^{(3)}=\chi_2$ for $y<0$. When such an interface is brought into the excitation volume, the destructive interference near O' is no longer complete due to the presence of two different $\chi^{(3)}$s on either side of the optical axis. In case the excitation volume is scanned across the $\chi^{(3)}$ edge, which is parallel to the phase jump in the excitation volume, it is expected that only the interface is highlighted while the rest of the CARS image remains dark. On the other hand, if the interface were to be introduced perpendicularly, i.e., with $\chi^{(3)}=\chi_1$ for $x>0$ and $\chi^{(3)}=\chi_2$ for $x<0$, then the resulting CARS image would appear dark with no enhancement of the interface. This is because one can always find at the focal plane two equally spaced points on either side of the optical axis, which interfere destructively near the far-field point O'. The above discussion illustrates that by shaping the phase distribution of the CARS signals in the focal volume, direction-specific and spectroscopically relevant interface enhancement or suppression is possible.

To generate a π-phase jump in the CARS field at the focal volume, the definite phase relationship among the CARS, the pump, and the Stokes fields ($\phi_c = 2\phi_p - \phi_S$) has to be considered. Based on this relation, it is clear that a π-phase jump in the Stokes field leads to a corresponding π-phase discontinuity in the generated CARS field. (Note that this is not true in the case of the pump beam due to the multiplicative factor of 2 in the phase relationship.)

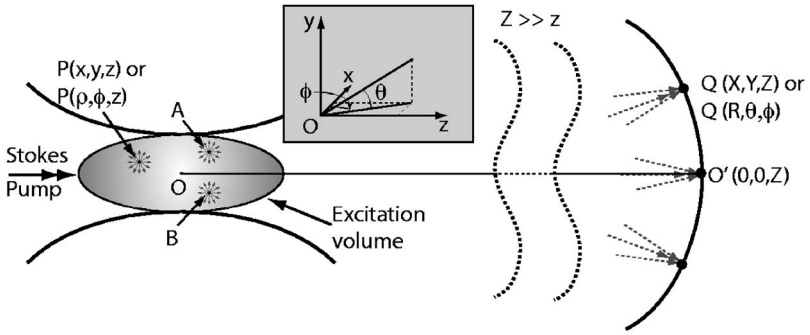

Fig. 1. Simple sketch of CARS generation showing the $y-z$ cross section of the excitation volume. $\overline{OO'}$ represents the optical axis with O being the origin of the coordinate system and also the center of the focal volume, and O' being a far-field point on the optical axis. The coordinates of the points in the near field are represented by (x,y,z) and those of the points in the far field by (X,Y,Z) in the Cartesian coordinate system. The outgoing arrows around the near-field points represent the CARS waves generated due to the local excitation, and the incoming arrows at the far-field points (O' and Q) represent the contribution of the electric field amplitudes from the individual points in the excitation volume.

The simplest technique to engineer this phase distribution in the focal volume of the Stokes beam is to employ higher-order Hermite–Gaussian input modes, HG10 and HG01. Experimentally, these higher-order modes can be generated from freely propagating Gaussian beams by using amplitude or phase edges.[28–30] Hence, in this paper, assuming a Gaussian pump beam, we investigate the effects of three different field distributions, namely, Hermite–Gaussian modes HG01 and HG10, and linearly polarized donut mode LG01, of the Stokes beam on the CARS output. In the following sections, we show, based on numerical calculations, that the first two field distributions enable the suppression of the interfaces that are parallel to the x and y axes, respectively, and that the latter highlights arbitrarily oriented interfaces in the plane of focus.

Though the discussion in the rest of this paper pertains to detecting the interfaces in the lateral plane, with an appropriate choice of the focal-field distribution, the analysis presented here can be easily extended to the detection of the chemical edges along the longitudinal direction as well.

3. REVIEW OF THE THEORY OF CARS IMAGE FORMATION

The general theory of local CARS generation, field propagation, and net CARS intensity detection is well studied.[8,9] Here we extend the theory to incorporate the effects of CARS excitation fields with alternative phase profiles as modeled by the first-order Hermite–Gaussian wavefronts based on a vectorial approach.

In a typical CARS microscope, a high numerical aperture objective lens is used to focus the pump and the Stokes fields to generate the excitation field. Both the pump and the Stokes beams are assumed to be monochromatic (picosecond CARS) and polarized along the x direction. For a given spatial distribution of the pump and the Stokes beams, the corresponding focal fields can be calculated based on the theory of angular spectrum representation introduced by Richards and Wolf.[31] Denoting the focal field of the pump beam as $\mathbf{E}_p(\mathbf{r})$ and that of the Stokes beam as $\mathbf{E}_S(\mathbf{r})$, the induced third-order nonlinear polarization, $\mathbf{P}_c(\mathbf{r})$, at the CARS wavelength is given in the tensorial notation as[9]

$$P_{ci}(\mathbf{r}) = \sum_{j,k,l} \chi^{(3)}_{ijkl}(\mathbf{r}) E_{pj}(\mathbf{r}) E_{pk}(\mathbf{r}) E^{*}_{Sl}(\mathbf{r}), \tag{1}$$

where $\chi^{(3)}(\mathbf{r})_{ijkl}$ $(i,j,k,l=1,2,3)$ are the components of the third-order susceptibility tensor of the sample. Since both the incident beams are polarized along the x direction, the dominant polarization component of $\mathbf{P}_c$ is also along the same direction with negligible contributions from the off-axis tensor components. However these neglected terms become important in techniques (such as polarization-sensitive CARS) where the incident polarization of the Stokes and the pump beams are different. Second, comparing the magnitudes of the orthogonal polarization components, we note that the magnitude of the y component is negligible; however the z-polarization component can be comparable to that of the x component for the higher-order beam modes. While this longitudinal component plays a major role in near-field detection methods, its contribution is of limited importance in the present case, where the CARS signal is detected in the far field.

The induced polarization in the excitation volume can be considered as a collection of radiating dipoles. The net CARS amplitude at any far-field point Q with coordinates $\mathbf{R} \equiv (X,Y,Z) \equiv (R,\theta,\phi)$ is a sum of the amplitude contributions from all these dipoles and is given by[12]

$$\mathbf{E}(\mathbf{R}) = -\int_{\mathcal{V}} \frac{e^{ik_c|\mathbf{R}-\mathbf{r}|}}{4\pi|\mathbf{R}-\mathbf{r}|^3}(\mathbf{R}-\mathbf{r}) \times [(\mathbf{R}-\mathbf{r}) \times \mathbf{P}_c(\mathbf{r})] \mathrm{d}^3\mathbf{r}, \tag{2}$$

where k_c is the magnitude of the wave vector of the CARS field and $\mathcal{V}$ is the excitation volume. In the above formula, the integrand corresponds to the contribution of the field at $\mathbf{R}$ due to a radiating dipole at a coordinate point $\mathbf{r}$ in the focal volume. The total CARS intensity for a given position (x,y,z) of the sample is obtained by integrating the intensities at the far-field plane within the acceptance angle $(\theta_{\max})$ or the numerical aperture of the detecting lens system. To calculate two- or three-dimensional images, the sample is displaced, and the above process is repeated for each position of the sample.

A. Focus Engineering of the Stokes Beam

In the last two paragraphs, we presented a general numerical procedure for the calculation of the far-field CARS radiation pattern and the CARS images for arbitrary focal field distributions of the Stokes and the pump beams. The field distribution near the focus of a high numerical aperture microscope objective due to arbitrary fields at its entrance plane can be calculated based on the angular spectrum representation method.[31] The resulting expression consists of three double integrals, with integration spanning over the azimuthal and the polar angles, corresponding to the three components of polarization at the focus. For the case of the Hermite–Gaussian input profiles, these double integrals reduce to single integrals.[12]

In this paper, we define conventional CARS excitation as illumination of the sample with tightly focused HG00 Stokes and HG00 pump fields. The higher-order excitations correspond to HG01, HG10, and LG01 Stokes fields combined with a HG00 pump field. Assuming no index mismatch and neglecting linear dispersion,[9] the focal fields for the Hermite–Gaussian modes, HG00, HG01, and HG10 as derived by Novotny and Hecht[12] are

$$\mathbf{E}_{00} = E_0 e^{-ikf} \begin{pmatrix} I_{00} + I_{02}\cos 2\phi \\ I_{02}\sin 2\phi \\ -2iI_{01}\cos\phi \end{pmatrix}, \tag{3}$$

$$\mathbf{E}_{01} = E_0 e^{-ikf} \begin{pmatrix} iI_{11}\cos\phi + iI_{14}\cos 3\phi \\ -iI_{12}\sin\phi + iI_{14}\sin 3\phi \\ -2I_{10} + 2I_{13}\cos 2\phi \end{pmatrix}, \tag{4}$$

$$\mathbf{E}_{10} = E_0 e^{-ikf} \begin{pmatrix} i(I_{11} + 2I_{12})\sin\phi + iI_{14}\sin 3\phi \\ -iI_{12}\cos\phi - iI_{14}\cos 3\phi \\ 2I_{13}\sin 2\phi \end{pmatrix}, \quad (5)$$

respectively, to within complex constant factors. In the above equations, the quantities I_{mn} ($m=0,1$ and $n=0,\ldots,4$) are one-dimensional integrals with respect to the polar angle and are given by

$$I_{mn}(\rho,z) = \int_0^{\theta'_{\max}} f_w(\theta)\sqrt{\cos\theta}\, g_{mn}(\theta) J_l(k\rho\sin\theta) e^{ikz\cos\theta} \sin\theta \, d\theta, \quad (6)$$

where $l=n$ if $n \leqslant m$, and $l=n-m$ if $n>m$ and $g_{0n}=1+\cos\theta$, $\sin\theta$, $1-\cos\theta$ for $n=0,1,2$ and $g_{1n}=\sin^2\theta$, $\sin\theta(1+3\cos\theta)$, $\sin\theta(1-\cos\theta)$, $\sin^2\theta$, $\sin\theta(1-\cos\theta)$ for $n=0,1,2,3,4$, respectively, $\theta'_{\max}$ is the acceptance angle of the focusing objective, which is assumed to be 60° (corresponding to a numerical aperture of 1.1 for a water immersion objective) and $\rho=(x^2+y^2)^{1/2}$. The function $f_w(\theta)$ is the apodization function[12] and is chosen to be one in our simulations. The focal field due to the LG01 mode, $\mathbf{E}_{\mathrm{LG}}(\mathbf{r})$, is calculated using the relation $\mathbf{E}_{\mathrm{LG}}=\mathbf{E}_{01}+i\mathbf{E}_{10}$.[12]

B. Strategy for Numerical Simulations

In the following numerical simulations, we assume the wavelength, λ_p, of the pump beam to be 800 nm and that of the Stokes, λ_S, to be 1064 nm. The strategy for numerical calculations is as follows:

1. Calculation of the focal fields: The focal volume of size 3 μm × 3 μm × 6 μm centered around the origin is divided into a three-dimensional grid of spacing 50 nm along each direction. The three-dimensional complex focal distribution of the pump and Stokes beams are calculated based on Eqs. (3)–(5). The pump field distribution, $\mathbf{E}_p(\mathbf{r})$ is calculated from Eq. (3) by setting $k=k_p$, whereas the Stokes field is calculated, depending on the application, from one of the three expressions for the Hermite–Gaussian modes by setting $k=k_S$. The one-dimensional integration of the quantities I_{mn} are computed numerically using adaptive quadrature algorithms.[32] Figure 2 shows the x component of the calculated focal amplitude and phase of the Stokes beam corresponding to HG00, HG01, HG10, and LG01 input modes. The phase discontinuities depicted in these images directly translate to equivalent phase jumps in the induced CARS excitation according to Eq. (1).

2. Calculation of the CARS polarization: Based on the focal fields obtained from the previous step, the three-dimensional induced nonlinear polarization, $\mathbf{P}_c(\mathbf{r})$, at the CARS wavelength is calculated using Eq. (1). As far as the nonlinear susceptibility $\chi^{(3)}$ is concerned, the bulk medium is assumed to be nonresonant, and the objects under investigation, semi-infinite interfaces, a right-angled corner or a spherical particle [shown in Figs. 3(a)–3(d)], are assumed to be resonant. Hence the third-order susceptibility of the bulk, denoted by χ_2, is a real quantity, and that of the resonant object, denoted by χ_1, is complex. Assuming a single vibrational resonance, the spectral dependence of the resonant medium is taken to be

$$\chi_1 = \chi_{nr} + \frac{\mathcal{G}}{\omega_p - \omega_S - \omega_R + i\Gamma_R}, \quad (7)$$

where χ_{nr} is the nonresonant part, which is assumed to be equal to that of the bulk ($\chi_{nr}=\chi_2$), ω_R is the resonance frequency of the Raman mode, $\Gamma_R=10\ \mathrm{cm}^{-1}$ is the half-width at the half maximum of the resonance peak, and the constant $\mathcal{G}$ is chosen so that the magnitude of the resonant part is 2.5 times the nonresonant part when $\omega_p-\omega_S=\omega_R$. Figure 3(e) shows the normalized plots of $|\mathrm{Im}\{\chi_1\}|$ and $|\chi_1|^2$ corresponding to the Raman and the conventional CARS spectra. In this paper, except in Section 5 where we study the spectral dependence, the resonant material is assumed to be on-resonance (i.e., $\omega_R=\omega_p-\omega_S$) and hence, $\chi_1=\chi_2+i2.5\chi_2$.

3. Calculation of the radiation pattern: Once the CARS polarization at the focal volume is computed, the far-field radiation pattern is determined using Eq. (2). The total CARS intensity is computed from the radiation pattern by integrating over the acceptance cone, $\theta_{\max}$, of the detector system. In the following sections, we show that the acceptance angle of the detector system plays a major role in determining the contrast of the interface-enhanced CARS images. At this juncture, we consider two detection schemes—the coherent and the incoherent.[33,34] The coherent detection scheme involves integrating the far-field

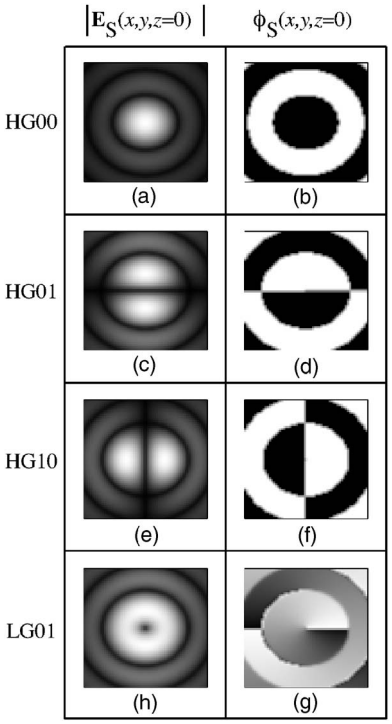

Fig. 2. x component of the focal amplitude distribution (left column) and the phase distribution (right column) of the Stokes beam with input HG00 mode, (a) and (b); HG01 mode, (c) and (d); HG10 mode, (e) and (f); and LG01 mode, (g) and (h). The size of each image is 3 μm × 3 μm. The gray values in the amplitude images are normalized with respect to that of the HG00 mode. The gray tone representation for the phase distribution is chosen such that the difference between the white and the black gray values is π rad in (b), (d), and (f) and 2π rad in (g).

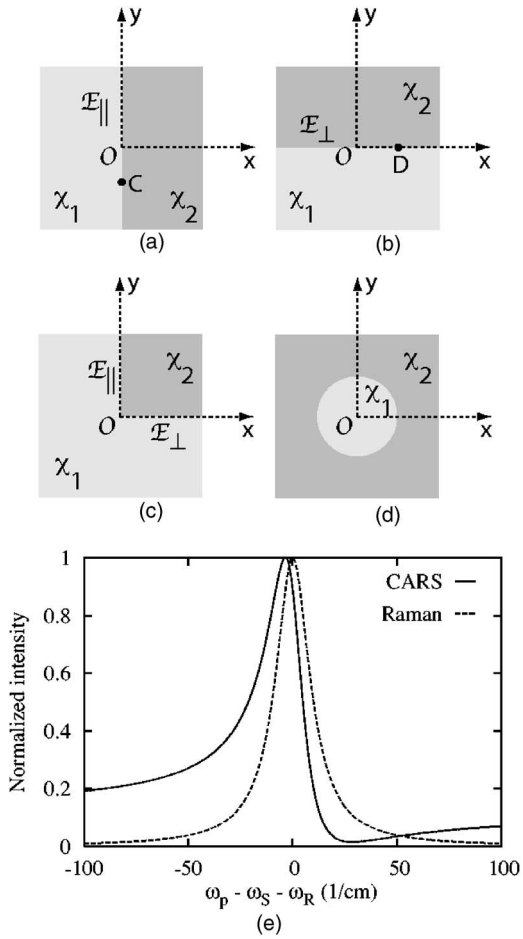

Fig. 3. Sketch of the objects being investigated: (a) an interface parallel to the y axis denoted as $\mathcal{E}_{\|}$, (b) interface perpendicular to the y axis denoted as $\mathcal{E}_{\perp}$, (c) right-angled corner with the edges being parallel and perpendicular to the y axis, (d) spherical particle of radius $r=500$ nm embedded in the bulk. χ_1 and χ_2 are the third-order nonlinear susceptibilities of the indicated regions and are assumed to be $\chi_1=2+5i$, and $\chi_2=2$ under the on-resonant condition. All the objects are assumed to be transparent and nonreflecting. (e) Assumed spectral dependence of χ_1—the solid curve: CARS spectrum, and the dashed curve: Raman spectrum.

radiation amplitude over the acceptance angle of the detection system. It can be realized experimentally by using a single-mode optical fiber for detecting the far-field radiation. On the other hand, the incoherent detection scheme involves integrating the far-field radiation intensity within the cone angle θ_{max}. Except in Section 6, where we compare the two schemes, only the experimentally easier incoherent detection scheme is analyzed.

4. Calculation of the intensity profiles and images: The CARS intensity (or interface) profiles and the two-dimensional CARS images are generated by repeating the above two steps for different lateral positions of the interface with respect to the origin in the focal volume.

4. LATERAL FOCUS SHAPING AND INTERFACE DETECTION: NUMERICAL RESULTS

In this section, we analyze the CARS radiation patterns and the images of four objects shown in Figs. 3(a)–3(d). The first two objects are semi-infinite interfaces formed between two materials with different third-order nonlinear susceptibilities oriented parallel [Fig. 3(a)] and perpendicular [Fig. 3(b)] to the y axis and denoted as $\mathcal{E}_{\|}$ and $\mathcal{E}_{\perp}$, respectively. These two sample configurations provide an intuitive understanding of the effect of focal-field engineering on the far-field CARS radiation intensity. We further analyze the CARS images from objects with interfaces in both lateral directions. In particular, we study the conventional and the focus-engineered CARS images of a right-angled corner [Fig. 3(c)] formed between two orthogonal sharp interfaces oriented with the edges parallel to the coordinate axes and a resonant spherical particle of radius 500 nm [Fig. 3(d)]. The analysis of these elementary sample configurations help to understand the focus-engineered CARS images of complex biological samples.

A. Radiation Pattern: Bulk

Before analyzing the interface detection in one and two dimensions, we first examine the effect of focus-engineered excitation on the CARS radiation pattern from a homogeneous bulk medium. Figure 4(a) shows the angular dependence of the far-field radiation pattern under conventional excitation. As discussed in Section 2, the intensity is maximum along the optical axis ($\theta=0°$) and reduces gradually for larger angles before going to zero at $\theta=90°$.

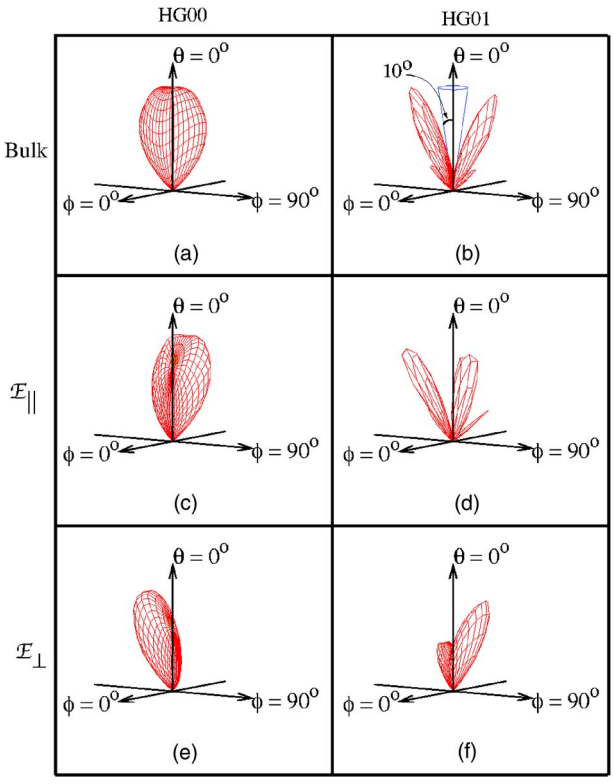

Fig. 4. (Color online) Comparing the far-field CARS radiation pattern from the bulk, (a) and (b); the $\mathcal{E}_{\|}$, interface, (c) and (d); and the $\mathcal{E}_{\perp}$ interface, (e) and (f) under conventional excitation (left column) and HG01 excitation (right column); θ and ϕ are the polar and the azimuthal angles. The directions $\phi=0$ and $\phi=90°$ correspond to the positive x and y directions. The acceptance angle of detection, $\theta_{max}=10°$, is indicated in (e).

Figure 4(b) shows the influence of HG01 excitation on the CARS radiation pattern from the bulk. Note that the intensity along the optical axis is negligibly small in contrast to the case of conventional excitation. This is a direct consequence of the destructive interference among the CARS waves generated at two distinct points (such as A and B in Fig. 1) in the focal volume, which are equally spaced on either side of the optical axis. However, for nonzero polar angles, the destructive interference is not complete due to the different optical path lengths traveled by the waves generated on either side of the π-phase jump in the focal volume. The radiation intensity reaches a maximum at an angle of $\theta=31.5°$, which (the angle) depends on the numerical aperture of the lens and the wavelength of the Stokes beam. In the incoherent detection scheme, for a given location of the excitation field in the sample, the net CARS intensity is obtained by integrating the far-field radiation intensity over a small cone angle [as indicated in Fig. 4(b) where the half-cone angle is drawn at 10°] about the optical axis. Thus in the case of HG01 excitation, the net CARS intensity would be close to zero, even though the bulk medium is highly resonant.

Although the form of the radiation pattern shown in Fig. 4(b) resembles that of the patterns published in the literature on second-harmonic and third-harmonic generation microscopy,[35–37] it is important to note the difference in their physical origin. In multiharmonic microscopy techniques, it is the Gouy phase shift, being larger than π rad, that gives rise to similar patterns for specific sample configurations. On the other hand, in conventional as well as lateral focus-engineered CARS microscopy, the Gouy phase shift is less than π rad and has limited impact on the forward-propagating CARS signal. Rather than resulting from the Gouy phase shift, the pattern in Fig. 4(b) is a direct consequence of the lateral phase shaping of the CARS excitation.

B. Interface Detection: One-Dimensional Interfaces

We next compare the CARS radiation patterns from the points located at one-dimensional chemical interfaces under conventional and HG01 excitations. We consider interfaces that are either parallel or perpendicular to the π-phase jump in the focal volume. Figures 4(c) and 4(e) show the radiation patterns from the points C [a point on the $\mathcal{E}_{\parallel}$ interface; see Fig. 3(a)] and D [a point on the $\mathcal{E}_{\perp}$ interface; see Fig. 3(b)] with conventional excitation. Both the patterns are tilted with the direction of maximum intensity being in the region of larger magnitude of $\chi^{(3)}$. The amount of the tilt is determined by the phases of the nonlinear susceptibilities, χ_1 and χ_2, on either side of the interface. The important point to note in these figures is that the CARS intensity along the optical axis, though less than that of the bulk, is nonzero for both the interfaces.

On switching to HG01 excitation, significant differences in the radiation patterns are evident. Most importantly, along the optical axis, the radiation pattern from point C [Fig. 4(d)] is negligibly small; on the contrary, the intensity from D [Fig. 4(f)] along the optical axis is comparable with the maximum intensity in the pattern. The radiation pattern from C is determined by the destructive interference of similar signals from either side of the phase jump. On the other hand, the emission pattern from D exhibits incomplete destructive interference because of the presence of two spectroscopically different materials across the phase jump. Hence, the far-field intensity along the optical axis from point D is nonzero.

On careful examination of the patterns from the $\mathcal{E}_{\perp}$ interface, one notices an apparently surprising feature: the maximum of the radiation pattern under HG01 excitation appears in the region of lower magnitude of $\chi^{(3)}$ in contrast to the pattern obtained using HG00 excitation. This observation can be qualitatively explained by considering the CARS emission of two equidistant points from the optical axis, such as A (located in the region of χ_2) and B (located in the region of χ_1), as shown in Figs. 1 and 3(b). The CARS intensity at a far-field point $Q(0,Y,Z)$ close to the optical axis (i.e., $|Y| \ll Z$) results from the interference of the waves generated from the points A and B. Assuming their separation to be d and rewriting $\chi_1=|\chi_1|e^{i\phi_1}$ (where $0 \leqslant \phi_1 \leqslant \pi$), the interference intensity can be approximated as

$$I_{AB} \propto |\chi_2 \pm |\chi_1| e^{i[\phi_1 + k_c d(Y/Z)]}|^2$$
$$\propto |\chi_1|^2 + |\chi_2|^2 \pm 2|\chi_1||\chi_2| \cos\left(\phi_1 + k_c d \frac{Y}{Z}\right), \qquad (8)$$

where the positive and the negative signs in the above expressions correspond to conventional and HG01 excitations, and the phase factor $k_c d(Y/Z)$ corresponds to optical path length difference between the two signals. The negative sign in the above expressions plays a major role in influencing the symmetry of the radiation pattern. From Eq. (8), it follows that under HG01 excitation, for $\phi_1 \neq 0$ or π, the far-field CARS intensity is higher for positive values of Y and lower for the negative values. On the other hand, under conventional excitation, the opposite is true: the CARS intensity is higher for the negative values of Y and lower for the positive values. This explains the asymmetry and the apparent discrepancy between the radiation patterns shown in Figs. 4(e) and 4(f). However, in either case, this asymmetry disappears when both the media in the sample are completely nonresonant, i.e., when $\phi_1=0$.

Figure 5(a) shows a plot of the net CARS intensity versus the lateral position of the excitation with respect to the chemical edge. The CARS intensity is calculated by integrating the radiation intensity over a cone angle of $\theta_{\max}=10°$, which is equivalent to a (detection) numerical aperture of ≈ 0.2 in air. The solid curve in the plot corresponds to the interface shown in Fig. 3(b) with the excitation spot being scanned along the y axis, and the dashed curve corresponds to the interface shown in Fig. 3(c) with the excitation spot being scanned along the x axis. As before, HG01 excitation is assumed in generating these plots. Due to this particular choice of the excitation field distribution, the maximum CARS intensity from the $\mathcal{E}_{\parallel}$ interface is approximately 50 times weaker than that from the $\mathcal{E}_{\perp}$ interface. The strong peak in the $\mathcal{E}_{\perp}$ intensity profile indicates the presence of an interface that is parallel to the phase jump in the excitation.

In Fig. 5(a), the plot corresponding to $\mathcal{E}_{\perp}$ shows, apart from a strong central peak, two secondary peaks. These

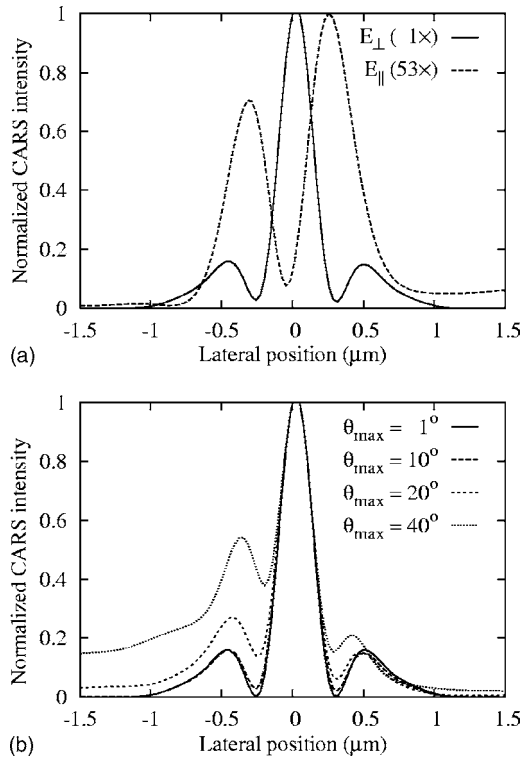

Fig. 5. (a) Far-field CARS intensity profiles obtained by scanning the HG01 excitation spot along the y axis across the $\mathcal{E}_\perp$ interface (solid curve) and along the x axis across the $\mathcal{E}_\parallel$ interface (dashed curve) with the acceptance angle of detection being 10°. (b) Dependence of the CARS intensity of the $\mathcal{E}_\perp$ interface on the acceptance angle θ_{max} under HG01 excitation.

secondary peaks can be suppressed by reducing the detection aperture. Figure 5(b) shows the influence of θ_{max} on the CARS intensity profile. For larger acceptance angles, in addition to the appearance of large secondary peaks, the background is nonzero. On the other hand, for smaller opening angles, though the absolute intensity reduces, the background intensity from the bulk is suppressed. Thus, in the incoherent detection scheme, one has to strike a compromise between the suppression of the secondary peaks and strength of the signal. The contrast can be improved by using the coherent detection scheme, as discussed in Section 6.

C. Interface Detection: Two-Dimensional Interfaces

In this subsection, we present the numerical results of detecting the interfaces along both x and y directions. This is achieved by choosing the profile of the input Stokes beam to be that of a Laguerre–Gaussian mode, LG01. For comparison, we also present the simulation results with HG01 and HG10 excitations.

Figure 6(a) shows the simulated CARS images of a right-angled corner [sketched in Fig. 3(c)] formed between the edges $\mathcal{E}_\parallel$ and $\mathcal{E}_\perp$ under conventional excitation. As expected, the resonant part of the image with larger amplitude of third-order susceptibility is brighter than the nonresonant part. On the other hand, under HG01, HG10, or LG01 excitations, the resulting CARS images [Figs. 6(c), 6(e), and 6(g), respectively] appear significantly different with only the chemical edges being highlighted, and the homogeneous background (both from the resonant and the nonresonant parts of the sample) being suppressed. The appearance of the secondary intensity maxima (away from the location of the edges) is a consequence of incoherent detection and can be suppressed by coherent detection schemes.

Figure 6(b) shows the conventional CARS image of a resonant spherical particle [sketched in Fig. 3(d)] embedded in a nonresonant bulk medium using Gaussian pump and Stokes beams. Clearly the particle is brighter than the background. The focus-engineered CARS images are shown in Figs. 6(d), 6(f), and 6(h). With HG01 and HG10 excitations, due to the specific geometry of these focal distributions, only parts of the interface are visible. However under LG01 excitation [Fig. 6(h)], the entire interface, the rim of the particle, is highlighted, and the bulk information from both the nonresonant background as well as from the central portion of the resonant particle is suppressed. The use of LG01 excitation, which is a linear combination of HG01 and H10 modes, clearly enhances the contrast of arbitrarily oriented interfaces in the lateral plane.

5. SPECTRAL DEPENDENCE

To investigate the spectral dependence, the excitation frequency, $\omega_p - \omega_S$, has to be detuned from the vibrational resonance frequency of the material. However, a change in the wavelength of the pump or the Stokes beams leads

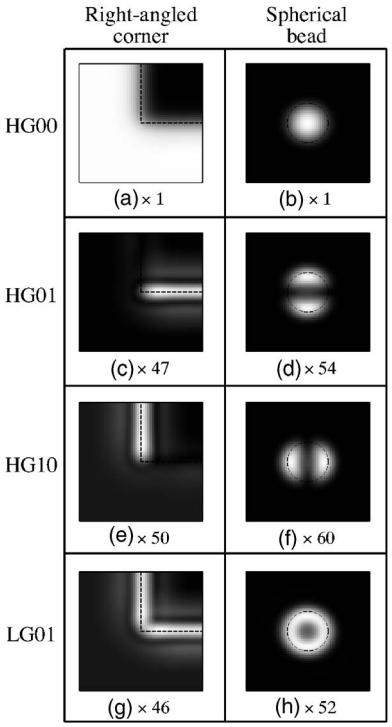

Fig. 6. CARS images of a right-angled corner (left column) and a resonant spherical bead of radius 500 nm (right column). Conventional excitation, images (a) and (b); HG01 excitation, images (c) and (d); HG10 excitation, images (e) and (f); LG01 excitation, images (g) and (h). The image size is 3 μm × 3 μm; the thin dotted lines in each image indicate the interface. The gray values of the images are normalized with respect to that of the conventional image in the corresponding column, and the respective normalization factors are indicated in the captions.

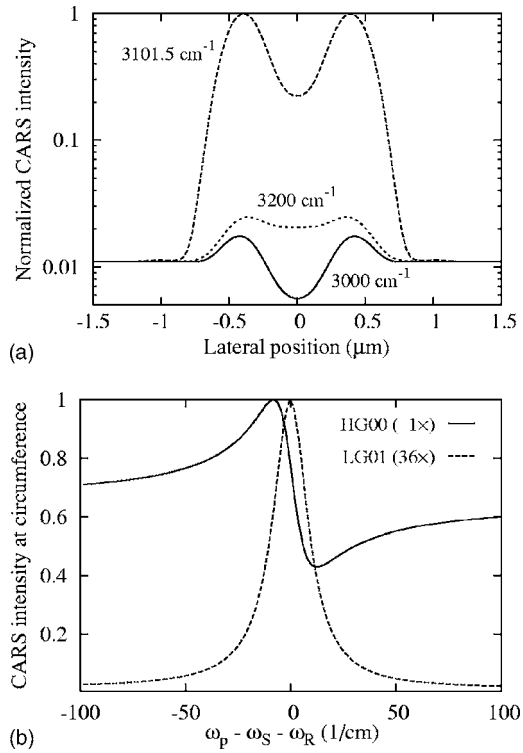

Fig. 7. (a) Spectral dependence of the intensity profiles of a bead of radius 500 nm under LG01 excitation. (b) The spectral variation of the output intensity at the circumference of the particle whose nonresonant susceptibility is the same as that of the bulk medium—the solid curve corresponds to conventional excitation, and the dashed curve corresponds to LG01 excitation. Note the change in the output spectral characteristics by a mere change of the spatial field distribution of the excitation.

to changes in the focal-field distribution, and the focal spot size, which, in turn, influence the generated CARS intensity patterns. Though these variations are small (less than 1%) in the desired range of ± 100 cm^{-1} around the vibrational resonance, it is instructive to study the influence of the spectral changes decoupled from the effects of focal spot variations. Here we analyze the spectral characteristics of the focus-engineered CARS signal by modifying the resonance frequency ω_R of the material while retaining the wavelengths of the pump and the Stokes beams at 800 and 1064 nm. For this setting, the difference frequency $\omega_{ex}=\omega_p-\omega_S$ corresponds to 3101.5 cm^{-1}. Figure 7(a) shows the intensity profiles of a bead of radius 500 nm along the y direction with LG01 excitation for three different frequencies ω_R. The CARS intensity at the interface is larger for the on-resonant condition (i.e., $\omega_{ex}=\omega_R=3101.5$ cm^{-1}) than for the off-resonant conditions. Also, if the excitation frequency is on the blue side of the resonance (i.e., $\omega_{ex}>\omega_R=3000.0$ cm^{-1}), the intensity at the center of the particle is lower than the surrounding medium because of lower magnitude of $|\chi_1|\approx 1.5$. On the other hand, if the excitation frequency is on the red side of the resonance frequency (i.e., $\omega_{ex}>\omega_R=3200.0$ cm^{-1}), the contrast of the edge with respect to the center of the bead diminishes due to almost equal magnitudes of $|\chi_1|\approx 2.1$ and χ_2.

Another important consequence of focus-engineered CARS excitation is the possibility of obtaining a Raman-like spectrum from the chemical edges. Due to the specific phase distribution of LG01 excitation, the intensity detected at the interface, as suggested by Eq. (8), is proportional to $|\chi_1-\chi_2|^2$. Hence, under the conditions of well-separated vibrational transitions, and equal nonresonant contributions from both the resonant particle and the (nonresonant) surrounding medium, the CARS spectrum of the interface resembles the Raman spectrum. Figure 7(b) compares the variation of the intensity near the circumference of the particle as a function of frequency detuning $\omega_{ex}-\omega_R$ under conventional and LG01 excitations. The conventional output, as expected, exhibits the typical dispersive characteristics of the CARS signal from a sample with both resonant and nonresonant contributions. On the other hand, the LG01 output shows a remarkable similarity with the Raman spectrum shown in Fig. 3(e); the shape of the curve is Lorentzian with the maximum appearing at $\omega_p-\omega_S=\omega_R$. This result demonstrates that spatial phase shaping can favorably modify the spectral characteristics of the CARS output.

6. COHERENT VERSUS INCOHERENT DETECTION

The incoherent detection scheme considered so far involves integrating the far-field radiation intensity over the acceptance angle of the detection system. A drawback of incoherent detection is that a signal attenuating aperture is required to observe the unique features of focus-engineered CARS. The coherent detection scheme, on the

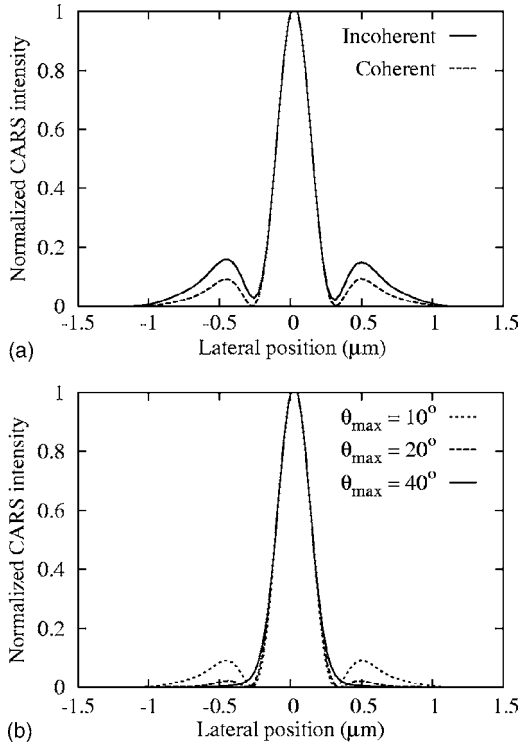

Fig. 8. (a) Comparison of the CARS intensity profiles of the $\mathcal{E}_\perp$ interface under HG01 excitation with incoherent (solid curve) and coherent (dashed curve) detection schemes; $\theta_{max}=10°$. (b) Dependence of the CARS intensity of the $\mathcal{E}_\perp$ interface on the acceptance angle θ_{max} under HG01 excitation employing the coherent detection scheme.

other hand, avoids the use of an aperture. It is accomplished with an amplitude or a field mode detector, such as a single-mode fiber, rather than an intensity detector. It has been used in confocal microscopy to improve the contrast of three-dimensional images.[33] Though experimentally more involved, the coherent detection scheme offers definite advantages in focus-engineered CARS microscopy. For example, under HG01 excitation, the radiation pattern from the bulk exhibits a double-lobed structure as shown in Fig. 4(b) with the two lobes being out-of-phase by π rad. Since such a pattern cannot excite propagating modes in a fiber detector, the output from the detector is (theoretically) zero. On the other hand, the radiation field from an interface (parallel to the x axis), does not average out at the detection aperture and hence results in a finite output intensity.

Figures 8(a) and 8(b) highlight some of the salient features of coherent detection when applied to the focus-engineered CARS technique. Figure 8(a) compares the intensity profiles from the $\mathcal{E}_\perp$ edge under HG01 excitation with coherent and incoherent detection schemes. Clearly, the secondary peaks are less intense under coherent detection. A complete suppression of these peaks is possible by increasing the acceptance angle of detection. Figure 8(b) compares the normalized CARS intensity profiles for three different acceptance angles of (coherent) detection. In contrast to the incoherent case [Fig. 5(b)], the secondary peaks are completely suppressed for $\theta_{\max}=40°$, even though the half-width of the intensity profile is the same. A second important feature of the coherent detection scheme is the suppression of the background from the homogeneous regions. Comparing Figs. 5(b) and 8(b), we note that in the coherent detection scheme, as a result of the integration of the field amplitude, the suppression of the background from the homogeneous regions is complete even for larger acceptance angles. As a consequence, the coherent scheme leads to greater output intensity (a factor of 3.6 for $\theta_{\max}=40°$) and thus to higher contrast interface images.

7. CONCLUSION

In this paper, we presented a systematic investigation of the application of the concept of focus engineering in picosecond CARS microscopy. We used spatial phase engineering of the focal CARS excitation field to enhance the detection of chemical interfaces in the lateral plane of focus along the forward direction. We demonstrated based on qualitative arguments and rigorous numerical simulations that the signal contribution from the homogeneous bulk in the sample can be suppressed, and only the information from the interfaces is retained for well-chosen phase-shaped focal fields. In particular, we showed that, in the plane of focus, one-dimensional interfaces can be detected using the Hermite–Gaussian modes, HG01 and HG10 and the two-dimensional interfaces using linearly polarized donut mode, LG01. The suppression of the bulk and the enhancement of the edges are direct consequences of the coherent nature of the CARS radiation. We determined that under conditions of equal nonresonant contributions from the resonant object and the (nonresonant) bulk, and well-separated resonances, the shape of the CARS spectrum of the interface under focus-engineered excitation resembles the Raman spectrum of the resonant medium. Even higher contrast from interfaces can be obtained when the coherent detection scheme is utilized in focus-engineered CARS microscopy.

Though the emphasis in this paper is on employing Hermite–Gaussian beams for the detection of the interfaces in the lateral dimensions, the concept of engineering the focal field for CARS excitation applies to the use of excitation fields with alternative phase profiles in general. We believe that the idea of combining focus engineering with CARS microscopy opens up exciting possibilities for high-resolution, high-contrast chemical imaging of interfaces in samples such as living cells and tissues. In addition, this work may trigger interest in exploring the use of unconventional excitation field distributions in various nonlinear coherent microscopy techniques.

Corresponding author E. O. Potma's e-mail address is epotma@uci.edu.

REFERENCES

1. J.-X. Cheng and X. S. Xie, "Coherent anti-Stokes Raman scattering microscopy: instrumentation, theory, and applications," J. Phys. Chem. B **108**, 827–840 (2004).
2. C. L. Evans, E. O. Potma, M. Puoris'haag, D. Côté, C. P. Lin, and X. S. Xie, "Chemical imaging of tissue in vivo with video-rate coherent anti-Stokes Raman scattering microscopy," Proc. Natl. Acad. Sci. USA **102**, 16807–16812 (2005).
3. H. Wang, Y. Fu, P. Zickmund, R. Shi, and J.-X. Cheng, "Coherent anti-Stokes Raman scattering imaging of axonal myelin in live spinal tissues," Biophys. J. **89**, 581–591 (2005).
4. X. Nan, E. O. Potma, and X. S. Xie, "Nonperturbative chemical imaging of organelle transport in living cells with coherent anti-Stokes Raman scattering microscopy," Biophys. J. **91**, 728–725 (2006).
5. C. Otto, A. Voroshilov, S. G. Kruglik, and J. Greve, "Vibrational bands of luminescent zinc(II)-octaethylporphyrin using a polarization-sensitive 'microscopic' multiplex CARS technique," J. Raman Spectrosc. **32**, 495–501 (2001).
6. A. Zumbusch, G. R. Holtom, and X. S. Xie, "Three-dimensional vibrational imaging by coherent anti-Stokes Raman scattering," Phys. Rev. Lett. **82**, 4142–4145 (1999).
7. E. O. Potma and X. S. Xie, "Detection of single lipid bilayers with coherent anti-Stokes Raman scattering (CARS) microscopy," J. Raman Spectrosc. **34**, 642–650 (2003).
8. E. O. Potma, W. P. de Boeij, and D. A. Wiersma, "Nonlinear coherent four-wave mixing in optical microscopy," J. Opt. Soc. Am. B **17**, 1678–1684 (2000).
9. J.-X. Cheng, A. Volkmer, and X. S. Xie, "Theoretical and experimental characterization of coherent anti-Stokes Raman scattering microscopy," J. Opt. Soc. Am. B **19**, 1363–1375 (2002).
10. J.-X. Cheng, A. Volkmer, L. D. Book, and X. S. Xie, "An epi-detected coherent anti-Stokes Raman scattering (E-CARS) microscope with high spectral resolution and high sensitivity," J. Phys. Chem. B **105**, 1277–1280 (2001).
11. A. Volkmer, J.-X. Cheng, and X. S. Xie, "Vibrational imaging with high-sensitivity via epidetected coherent anti-Stokes Raman scattering microscopy," Phys. Rev. Lett. **87**, 0239011 (2001).
12. L. Novotny and B. Hecht, *Principles of Nano-Optics* (Cambridge U. Press, 2006).

13. S. Hell and J. Wichmann, "Breaking the diffraction resolution limit by stimulated emission: stimulated-emission depletion fluorescence microscopy," Opt. Lett. **19**, 780–782 (1994).
14. T. A. Klar and S. Hell, "Subdiffraction resolution in far-field fluorescence microscopy," Opt. Lett. **24**, 954–956 (1999).
15. S. W. Hell and E. H. K. Stelzer, "Fundamental improvement of resolution with a 4Pi-confocal fluorescence microscope using two-photon excitation," Opt. Commun. **93**, 277–282 (1992).
16. A. Egner, S. Jakobs, and S. W. Hell, "Fast 100-nm resolution 3D-microscope reveals structural plasticity of mitochondria in live yeast," Proc. Natl. Acad. Sci. USA **99**, 3370–3375 (2002).
17. M. Dyba and S. W. Hell, "Focal spots of size $\lambda/23$ open up far-field fluorescence microscopy at 33 nm axial resolution," Phys. Rev. Lett. **88**, 163901 (2002).
18. S. Fürhapter, A. Jesacher, S. Bernet, and M. Ritsch-Marte, "Spiral phase contrast imaging in microscopy," Opt. Express **13**, 689–694 (2005).
19. W. P. de Boeij, J. S. Kanger, G. W. Lucassen, C. Otto, and J. Greve, "Waveguide CARS spectroscopy: a new method for background suppression, using dielectric layers as a model," Appl. Spectrosc. **47**, 723–730 (1993).
20. J. N. Gannaway and C. J. R. Sheppard, "Second-harmonic imaging in the scanning optical microscope," Opt. Quantum Electron. **10**, 435–439 (1978).
21. Y. Guo, P. P. Ho, H. Savage, D. Harris, P. Sacks, S. Schantz, F. Liu, N. Zhadin, and R. R. Alfano, "Second-harmonic tomography of tissues," Opt. Lett. **22**, 1323–1325 (1997).
22. P. J. Campagnola, M. Wei, A. Lewis, and L. M. Loew, "High-resolution nonlinear optical imaging of live cells by second harmonic generation," Biophys. J. **77**, 3341–3349 (1999).
23. L. Moreaux, O. Sandre, M. Blanchard-Desce, and J. Mertz, "Membrane imaging by simultaneous second-harmonic generation and two-photon microscopy," Opt. Lett. **25**, 320–322 (2000).
24. M. Müller, J. Squier, K. R. Wilson, and G. J. Brakenhoff, "3D-microscopy of transparent objects using third-harmonic generation," J. Microsc. **191**, 266–274 (1998).
25. J. A. Squier, M. Müller, G. J. Brakenhoff, and K. R. Wilson, "Third harmonic generation microscopy," Opt. Express **3**, 315–324 (1998).
26. D. Yelin and Y. Silberberg, "Laser scanning third-harmonic-generation microscopy in biology," Opt. Express **5**, 169–175 (1999).
27. D. Débarre, W. Supatto, E. Farge, B. Moulia, M.-C. Schanne-Klein, and E. Beaurepaire, "Velocimetric third-harmonic generation microscopy: micrometer-scale quantification of morphogenetic movements in unstained embryos," Opt. Lett. **29**, 2881–2883 (2004).
28. L. Novotny, E. J. Sánchez, and X. S. Xie, "Near-field optical imaging using metal tips illuminated by higher-order Hermite–Gaussian beams," Ultramicroscopy **71**, 21–29 (1998).
29. V. Delaubert, D. A. Shaddock, P. K. Lam, B. C. Buchler, H.-A. Bachor, and D. E. McClelland, "Generation of a phase-flipped Gaussian mode for optical measurements," J. Opt. A **4**, 393–399 (2002).
30. E. Engel, N. Huse, T. A. Klar, and S. W. Hell, "Creating $\lambda/3$ focal holes with a Mach–Zehnder interferometer," Appl. Phys. B **77**, 11–17 (2003).
31. B. Richards and E. Wolf, "Electromagnetic diffraction in optical systems II: Structure of the image field in an aplanatic system," Proc. R. Soc. London, Ser. A **253**, 358–379 (1959).
32. R. Piessens, E. de Doncker-Kapenga, C. W. Uberhuber, and D. K. Kahaner, *QUADPACK: A Subroutine Package for Automatic Integration* (Springer-Verlag, 1983).
33. T. Wilson and J. B. Tan, "Finite sized coherent and incoherent detectors in confocal microscopy," J. Microsc. **182**, 61–66 (1995).
34. P. Higdon, R. Juškaitis, and T. Wilson, "The effect of detector size on the extinction coefficient in confocal polarization microscopes," J. Microsc. **187**, 8–11 (1997).
35. L. Moreaux, O. Sandre, S. Charpak, M. Blanchard-Desce, and J. Mertz, "Coherent scattering in multi-harmonic light microscopy," Biophys. J. **80**, 1568–1574 (2001).
36. E. Y. S. Yew and C. J. R. Sheppard, "Effects of axial field components on second harmonic generation microscopy," Opt. Express **14**, 1167–1174 (2006).
37. J.-X. Cheng and X. S. Xie, "Green's function formulation for third-harmonic generation microscopy," J. Opt. Soc. Am. B **19**, 1604–1610 (2002).